Characteristics and formation processes of (Ba, K, NH$_4$)-feldspar and cymrite from a lower Cambrian black shale sequence in Anhui Province, South China

Chao Chang[1], Wen-Xuan Hu[1,*], Qi Fu[2], Jian Cao[1], Xiao-Lin Wang[1], Ye Wan[1] and Su-Ping Yao[1]

[1] State Key Laboratory for Mineral Deposits Research, Institute of Energy Sciences, School of Earth Sciences and Engineering, Nanjing University, Nanjing 210046, China

[2] Department of Earth and Atmospheric Sciences, University of Houston, Houston, TX 77204, USA

ABSTRACT

Barium-rich silicates were recently found in the lower Cambrian black shale sequence of Anhui Province, South China. The Ba silicates can be divided into Ba-poor K-feldspar, Ba-rich K-feldspar and cymrite, on the basis of occurrence and composition. The Ba-poor K-feldspar have low BaO contents (<1.00 wt.%) and occur as sporadic grains in mudstone. In contrast, the Ba-rich K-feldspar have higher BaO contents (1.36–20.51 wt.%) and occur mainly as rims around grains of Ba-poor K-feldspar in mudstone, as void fillings in dolostone, and as grains dispersed in chert. The cymrite is observed only in chert and occurs as dispersed euhedral tabular crystals. Analyses of the Ba-poor K-feldspar and Ba-rich K-feldspar provide compositions that total <100 wt.% and show non-stoichiometry characterized by $(Na + K + Ba + Ca)_{apfu}$ less than 1.00 and $(Al + Si)_{apfu}$ slightly higher than 4.00. Raman and infrared (IR) spectroscopy has revealed the presence of NH_4^+ and H_2O in the Ba-rich K-feldspar, which accounts for the unusual composition of these feldspars. We suggest that the formation processes of the Ba-poor K-feldspar, Ba-rich K-feldspar and cymrite were closely associated with multi-stage hydrothermal fluids enriched in Ba and NH$_4$, consistent with an extensional tectonic setting during the early Cambrian. The Ba-poor K-feldspars might have formed through interactions between pre-existing K-feldspars and hydrothermal fluids. The Ba-rich K-feldspars in mudstone and dolostone formed mainly by precipitation from hydrothermal fluids that infiltrated the sediments, and we suggest the Ba-rich K-feldspars and cymrite in the chert are of exhalative hydrothermal origin.

Keywords: Ba-poor K-feldspar, Ba-rich K-feldspar, cymrite, mineral characteristics, mineral formation processes, hydrothermal activity.

Introduction

Barium-rich feldspars are rare in nature. Barium is typically a minor constituent of common silicate minerals, but it can be enriched significantly in some contexts, especially in potassic rock-forming minerals such as K-feldspar and muscovite (e.g. Chabu and Boulègue, 1992; Raith *et al.*, 2014; Henry *et al.*, 2015). Ba-rich K-feldspars are typically associated with manganese–ferromanganese deposits (Viswanathan and Kielhorn, 1983; McSwiggen *et al.*, 1994), stratabound Ba-rich sulfide deposits (Fortey and Beddoe–Stephens, 1982; Chabu and Boulègue, 1992), baryte deposits (Moro *et al.*, 2001; Xia *et al.*, 2005; Han *et al.*, 2013), Ba-rich sedimentary or metasedimentary rocks (Reinecke, 1982; Jakobsen *et al.*, 1990; Deer *et al.*, 2001; Essene *et al.*, 2005; Raith *et al.*, 2014), and other Ba-rich rocks such as mafic xenoliths affected by Ba metasomatism (Henry *et al.*, 2015). The formation processes of Ba-rich K-feldspars commonly involve hydrothermal activity and low- to medium-grade metamorphism.

*E-mail: huwx@nju.edu.cn

In the lower Cambrian of South China, Ba-rich K-feldspars have been reported from the baryte deposits of Guizhou Province and the vanadium deposits of Jiangxi Province (Fig. 1) (Long *et al.*, 1994; Xia *et al.*, 2005; Han *et al.*, 2013). In the baryte deposits, Ba-rich K-feldspars occur either as cores surrounded by pyrite grains or as euhedral crystals in contact with quartz or baryte (Xia *et al.*, 2005; Han *et al.*, 2013). In the vanadium deposits, most of the Ba-rich K-feldspars occur as a major constituent of the host rocks, while some occur as clusters of lamellar crystals in amygdaloidal geodes (Long *et al.*, 1994). The Ba-rich K-feldspars in the baryte and vanadium deposits were identified as hyalophane, and are regarded as important evidence for the hydrothermal origin of the deposits, yet their origin has not been adequately discussed

(Long *et al.*, 1994; Xia *et al.*, 2005; Han *et al.*, 2013). Although Ba-rich feldspars in the vanadium deposits were identified as hyalophane by whole-rock X-ray diffraction, it is noteworthy that they have non-stoichiometric compositions characterized by abnormally high contents of SiO_2, based on the limited compositional data provided in those earlier studies. However, because no further investigations were undertaken, the formation mechanisms of the Ba-rich K-feldspars in the vanadium deposits, as well as the cause of their non-stoichiometry, remains unclear.

Recently, Ba-bearing silicates were found in drill cores of the lower Cambrian Hetang Formation in Anhui Province (Fig. 1). They were distributed across the whole formation, exhibiting complex occurrence patterns and unusual compositional features, thus
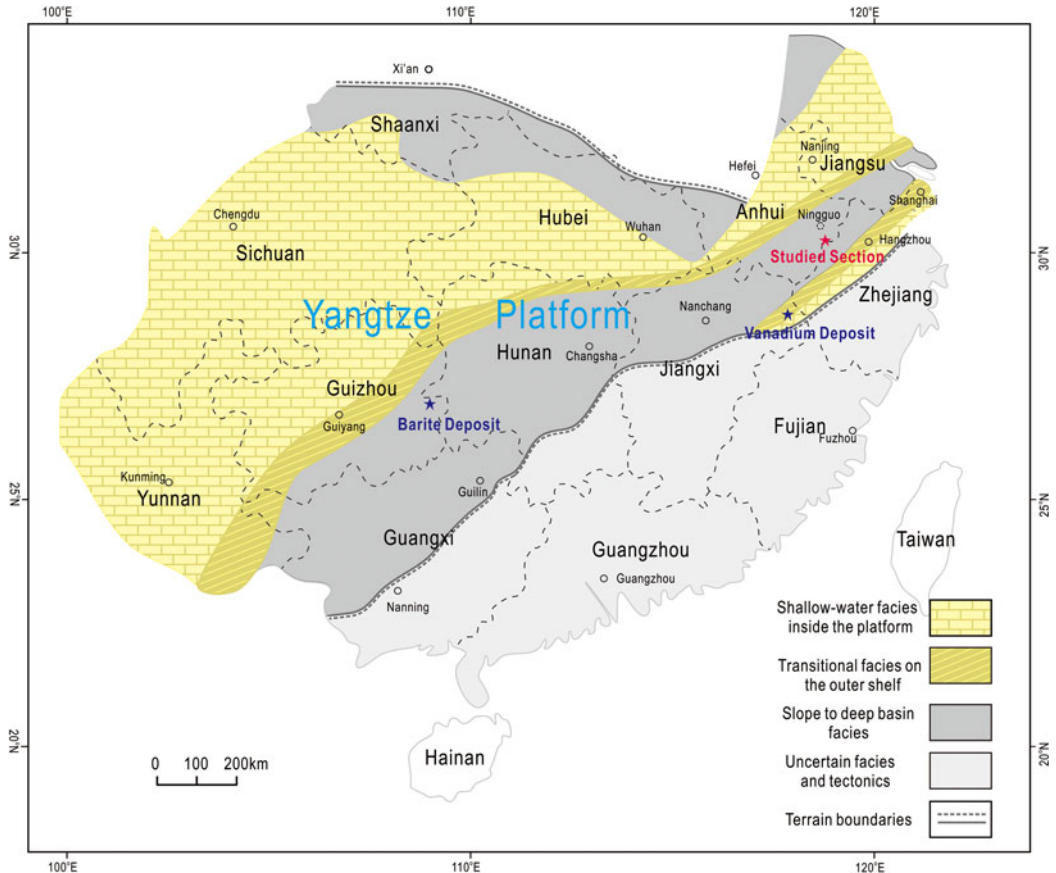

FIG. 1. Simplified palaeogeographic map of the Yangtze Platform in early Cambrian, modified after Jiang *et al.* (2007) and Chen *et al.* (2009). The location of the section studied is labelled in red, while locations of the baryte and vanadium deposits are also shown in blue (Xia *et al.*, 2005; Han *et al.*, 2013).

providing an excellent opportunity for further investigations of the characteristics and formation processes of Ba-bearing silicates in early Cambrian rocks of South China. The compositions of the Ba-rich silicates were analysed by electron microproy (EMP), scanning electron microscope (SEM) and Raman and infrared (IR) spectroscopy. The results demonstrate that the Ba-bearing silicates include cymrite and Ba-bearing K-feldspars with non-stoichiometric compositions. In this paper, we systematically characterize the occurrences and compositions of these Ba-bearing silicates, discuss the causes of the non-stoichiometry in the Ba-bearing feldspars, and establish the possible genesis of all these Ba-bearing silicates.

Geological setting

During the Ediacaran–Cambrian transition, the Yangtze platform gradually evolved from a rift into a passive continental margin basin under the influence of an extensional tectonic setting (Wang and Li, 2003; Chen *et al.*, 2009). The sedimentary sequences of the platform can be divided into three distinct facies: shallow water, transitional, and slope-to-deep basin (Fig. 1). Thick carbonate strata represent the shallow-water facies, whereas the slope-to-deep basin facies consists mainly of a series of interbedded black cherts and shales. The transitional facies consists of carbonates and black shales (Zhu, 2004; Jiang *et al.*, 2007).

The drillcore section of the Hetang Formation investigated in this study was recovered from Well Wanning 2 in Ningguo County, Anhui Province (Fig. 1). The sedimentary sequence is not metamorphosed, and comprises the Xijianshan, Hetang and Dachenling formations (Fig. 2). The top of the Xijianshan Formation is characterized by alternating dolostones and chert. The Xijianshan Formation is overlain by the Hetang Formation, and the boundary between the two can be identified by the disappearance of dolostone and the appearance of mudstone. The Hetang Formation is composed mainly of mudstone, including carbonaceous, siliceous, calcareous and dolomitic varieties. Thin layers of chert and limestone are also observed. The mudstones in the Hetang Formation are rich in organic matter with TOC contents of 2.10–27.13 wt.% (Chang *et al.*, 2016). The Hetang Formation is overlain by the Dachenling Formation, which consists mainly of limestone. Quartz and calcite veins are common in these strata, indicating strong fluid migration during diagenesis.

Samples and methods

Subsequent to thin section observations and specimen identification, 51 samples were selected for EMP analysis. Twenty-five samples containing Ba-bearing silicates are marked on the lithological column in Fig. 2, and quantitative compositional analyses were carried out on the Ba-bearing silicates in 16 of these samples. The samples cover the entire Hetang Formation and the top of the Xijianshan Formation. Rock types include mudstone, chert and dolostone. The mudstone samples are from throughout the Hetang Formation, while the chert and dolostone samples were collected from the bottom of the Hetang Formation and the top of the Xijianshan Formation, respectively (Fig. 2). Some of the samples were also investigated by SEM for morphological observations of the Ba-silicates. Raman and IR spectra of the Ba-rich K-feldspars were also acquired.

Compositions and back-scattered electron images of the Ba-rich silicates were obtained on polished, carbon-coated thin sections using a JEOL JXA-8100 electron microprobe at the State Key Laboratory for Mineral Deposits Research at Nanjing University, Nanjing, China. The analytical conditions, using three wavelength-dispersive crystal spectrometers, were a 15 kV accelerating voltage, a 20 nA beam current, and an electron spot focused to 1–2 µm. The counting time was 10 s on peak positions, and two times 5 s on background positions. The analytical standards included the following well-characterized natural and synthetic minerals: orthoclase for K and Si, albite for Na and Al, plagioclase for Ca, barium fluoride for Ba, MnTiO$_3$ for Mn, and hornblende for Mg and Fe.

Scanning electron microscope imaging was carried out on carbon-coated thin sections using a JSM-6490 scanning electron microprobe. The working conditions were an acceleration voltage of 20 kV, a temperature of 20°C and an air humidity of <50%.

The Raman spectra of the Ba-rich feldspars were acquired *in situ* with a Raman spectrometer (LabRAM HR800, Horiba) equipped with a charge coupled device (CCD) detector (1024 × 256 pixels, aircooled to –70°C) at Nanjing University. The conditions used for acquisitions included 532.11 nm (air-cooled, frequency-doubled Nd:YAG) laser excitation, a 50× Olympus objective, and a 1800 groove/mm grating with a spectral resolution of ∼1 cm^{-1}. Laser light (9.5 mW) was focused on the Ba-rich feldspar during the spectra measurements. CCD
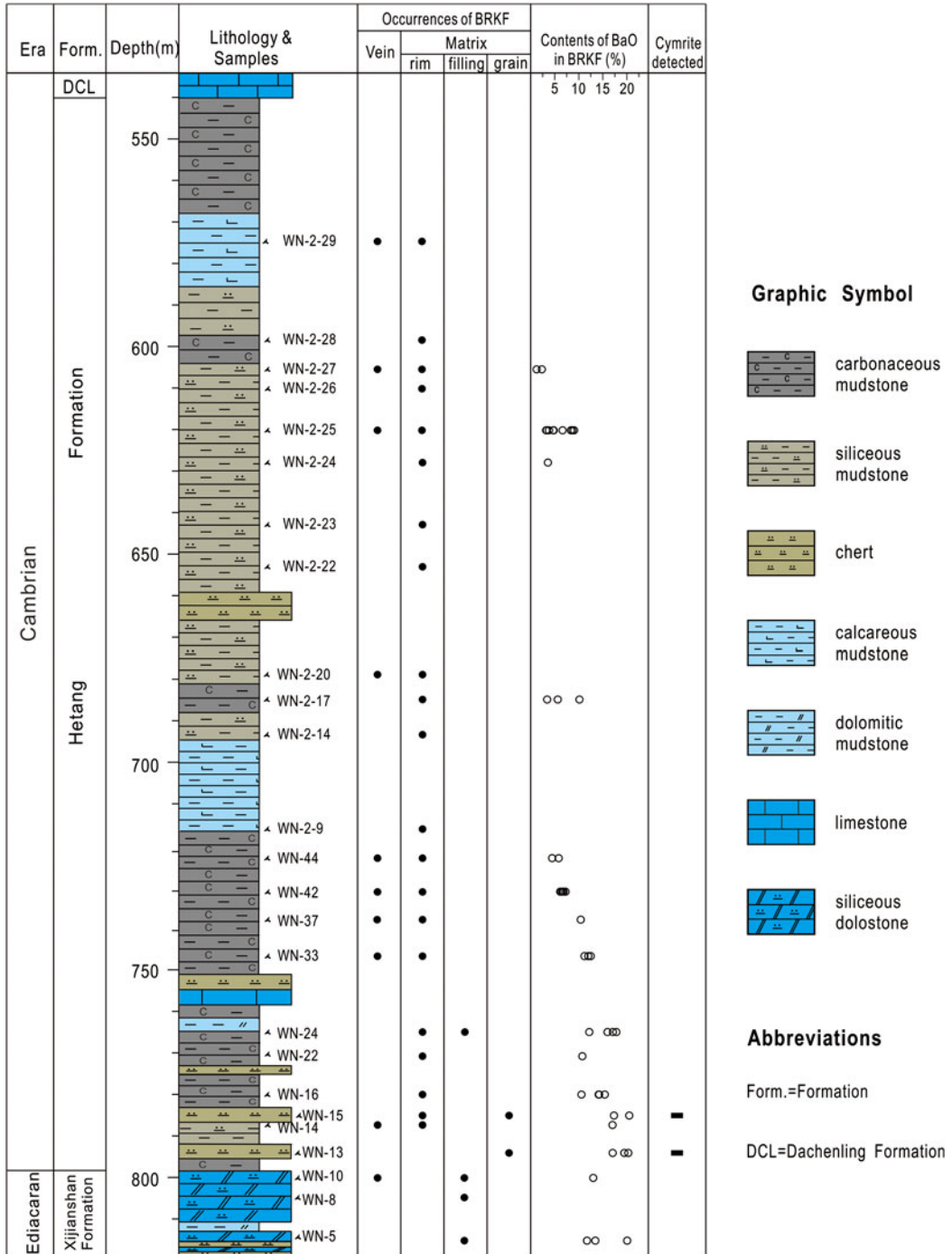
FIG. 2. Lithological column of the studied drillcore. The locations of representative samples, the occurrences of Ba-rich K-feldspar (BRKF), and the BaO contents of the Ba-rich K-feldspar are also shown.

spectra covering a whole wavenumber range of 100–4000 cm^{-1} were acquired first to configure the Raman signal range of the Ba-rich feldspars. The results indicated that the wavenumber range of the Ba-rich feldspars was ~100–3250 cm^{-1}, and further analyses with a wavenumber range of 100–3250 cm^{-1} were then carried out. The spectrometer was calibrated with the ν_1 band of silicon at 520.2 cm^{-1} (Parker *et al.*, 1967). Each spectrum was acquired for 60 s with three acquisitions.

Infrared experiments were performed using a Thermo Nicolet FTIR spectrometer coupled to a Nicolet Centaurμs FTIR microprobe with a reflection accessory at the Key Laboratory of Surficial Geochemistry, Ministry of Education, Nanjing University. The microprobe was equipped with a camera that provided an optical image (~20 μm × 20 μm) of the region sampled by IR. The spectra of analysed areas were recorded with left μscope reflection mode (%R) using a single element mercury cadmium telluride detector. The results were recorded as the average of 128 scans in the spectral range of 4000–650 cm^{-1} at a resolution of 8 cm^{-1}. Each spectrum was acquired following the withdrawal of a gold-coated glass substrate.

Results and discussion

Occurrences and compositions

Various occurrences of the Ba-bearing silicates were observed by back-scattered electron imaging, including sporadic discrete grains, rims on other minerals, void fillings and the components in veins. There is a close relationship between the occurrences and compositions of the various Ba-bearing silicates, allowing them to be divided into three types: Ba-poor K-feldspar; Ba-rich K-feldspar; and cymrite.

Ba-poor K-feldspar

The Ba-poor K-feldspars occur mainly as anhedral grains that are distributed sporadically in the matrix of the mudstones (Fig. 3). The grain sizes of the Ba-poor K-feldspars in most samples are less than or close to 10 μm (Fig. 3a), but reach ~30 μm in sample WN-16 from the base of the Hetang Formation (Fig. 3b–c).

Electron microprobe analyses of most of the Ba-poor K-feldspars provide compositions that total <100 wt.% (total range, 96.34–100.34 wt.%; Table 1). K$_2$O, SiO$_2$ and Al$_2$O$_3$ are the main components, with contents ranging from 9.25–16.09 wt.%, 64.36–67.41 wt.% and 18.36–19.27 wt.%, respectively. The low BaO contents of the Ba-poor K-feldspars are limited to a range of 0.10–1.00 wt.%. The Na$_2$O contents of the Ba-poor K-feldspars range from 0.04 to 0.45 wt.%. As shown in Fig. 4a, there is a strong negative linear correlation between K$_2$O and SiO$_2$ (Fig. 4a). In contrast, only a weak negative correlation can be recognized between BaO and SiO$_2$ (Fig. 4b).

Formulae calculations based on eight oxygen atoms indicate that most of the Ba-poor K-feldspars are non-stoichiometric. The values of $(Na + K + Ba)_{apfu}$ for the Ba-poor K-feldspars range from 0.56–0.98, while those of $(Al + Si)_{apfu}$ range from 4.00–4.11 (Table 1). Stoichiometric Ba-rich K-feldspars were only detected in sample WN-16, and these were accompanied by non-stoichiometric Ba-rich K-feldspars (Table 1).

Ba-rich K-feldspar

Ba-rich K-feldspars are observed in most of the samples, and their modes of occurrence vary among different rock types (Fig. 2). In the mudstones, Ba-rich K-feldspars occur mainly as rims that partly or completely surround Ba-poor K-feldspar grains (Fig. 3). The rims are thicker in sample WN-16 and are discontinuous where the Ba-poor K-feldspar grains are in contact with quartz or other minerals (Fig. 3b–c). In the dolostones, Ba-rich K-feldspars commonly occur together with quartz as void fillings (Fig. 5a). In the cherts, the Ba-rich K-feldspars are dispersed mainly in the matrix, and are several to ~30 μm in size (Fig. 5b). In addition, rectangular and rhombic Ba-rich K-feldspar aggregates of ~100–500 μm in size were observed in sample WN-24 (Fig. 5c), and quartz occur in the centres of some of these aggregates (Fig. 5c). Calcite grains are observed around all the aggregates (Fig. 5c).

Ba-rich K-feldspars have also been observed in cross-cutting veins where they occur together with quartz, and which are common in the mudstones and dolostones (Fig. 5d–f). The abundance of Ba-rich K-feldspar in different veins varies significantly. In most veins, the Ba-rich K-feldspars are anhedral or subhedral (Fig. 5d), but can be euhedral in other veins (Fig. 5e–f). The euhedral Ba-rich K-feldspar grains are weakly zoned in composition and are occasionally surrounded by (or connected with) Ba-rich K-feldspars with lower Ba contents (Fig. 5e–f). Notably, the Ba-rich K-feldspars in veins are commonly associated with Ba-rich K-feldspars in the matrix, indicating a genetic relationship between the two (Fig. 5d–e).

Electron microprobe analyses of most of the Ba-rich K-feldspars provide compositions that total
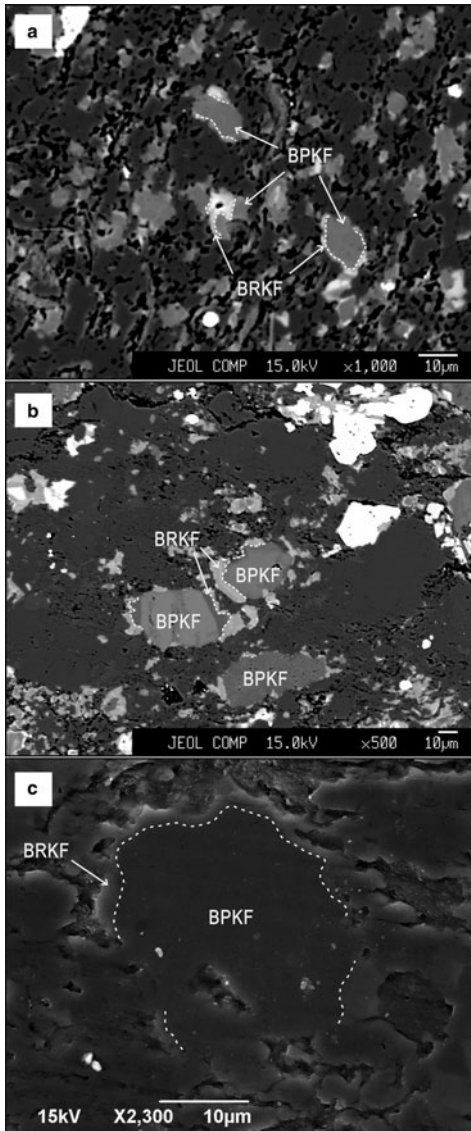
5

FIG. 3. Back-scattered electron (BSE) and secondary electron (SE) images showing the occurrences of Ba-poor K-feldspars in mudstones: (*a*) Ba-poor K-feldspars (BPKF) occur as scattered individual grains partly surrounded by Ba-rich K-feldspar (BRKF) rims, Sample WN-2-28; (*b*) larger Ba-poor K-feldspar grains (∼µm) are observed in Sample WN-16; (*c*) the Ba-rich K-feldspar rim is discontinuous where the Ba-poor K-feldspar grain is connected to other minerals, e.g. quartz, Sample WN-16.

<100 wt.% (total range, 96.08–99.10 wt.%; Table 1). BaO, K_2O, SiO_2 and Al_2O_3 are the main components, with contents ranging from

1.36–20.51 wt.%, 5.43–9.63 wt.%, 49.03–66.42 wt.% and 19.04–23.13 wt.%, respectively (Table 1). Different samples from the drilled profile show various ranges of BaO contents in the Ba-rich K-feldspars (Table 1; Fig. 2). Na_2O contents of the Ba-rich K-feldspars are <0.40 wt.% (Table 1).

Our analytical results for K_2O and SiO_2 in the Ba-rich K-feldspars, and the correlation between them (Fig. 6*a*), differ from those reported in most previous studies (Jakobsen, 1990; Chabu and Boulègue, 1992; McSwiggen *et al.*, 1994; Moro *et al.*, 2001; Xia *et al.*, 2005; Han *et al.*, 2013; Raith *et al.*, 2014; Henry *et al.*, 2015). As shown in Fig. 6*a*, our analyses give lower K_2O and higher SiO_2 contents, and the correlation between them is much weaker than reported previously. Interestingly, the compositions of the Ba-rich K-feldspars reported by both Long *et al.* (1994) and Orberger *et al.* (2005) are similar to our results. The BaO and SiO_2 contents of the Ba-rich K-feldspars in our samples show a strong linear correlation which resembles that reported in previous studies, regardless of the higher SiO_2 contents in the present study (Fig. 6*b*).

The formulae calculated in this study indicate that the Ba-rich K-feldspars have non-stoichiometric compositions: the value of $(Na + K + Ba)_{apfu}$ varies from 0.57 to 0.87, while that of $(Al + Si)_{apfu}$ ranges from 4.03 to 4.11. The correlation between the $(Na + K)_{apfu}$ and Si_{apfu} values of the Ba-rich K-feldspars in our samples differs from that reported in most previous studies. As shown in Fig. 6*c*, the data points from most previous studies are closely distributed along the theoretical line of hyalophane, while those from Long *et al.* (1994), Orberger *et al.* (2005) and the present study are distributed sparsely in a single area away from the line.

Cymrite

Cymrite is observed only in two chert samples (WN-13 and 15) from the base of the Hetang Formation (Fig. 2). It is associated with Ba-rich K-feldspar and occurs mainly in the form of ∼10 µm tabular crystals that are dispersed throughout the matrix (Fig. 5*a* and Fig. 7*a*). Furthermore, microcracks in the samples are filled with cymrite and Ba-rich K-feldspars, and the cymrite crystals locally overgrow the Ba-rich K-feldspar grains (Fig. 7*a*–*b*).

Electron microprobe analyses of the cymrite provide totals of <100 wt.% (total range, 94.94–95.70 wt.%; Table 1). BaO, SiO_2 and Al_2O_3 are the main components, with contents ranging from

6

TABLE 1. Representative compositions of Ba-poor K-feldspar, Ba-rich K-feldspar and cymrite.

Group	Ba-poor K-feldspar											
Sample	WN-2-28			WN-2-25			WN-2-24		WN-2-17	WN-44		WN-42
Na$_2$O	0.06	0.04	0.28	0.10	0.04	0.06	0.05	0.01	0.26	0.12	0.26	0.20
MgO	0.01	0.02	0.05	0.01	0.00	0.06	0.00	0.06	0.00	0.00	0.01	0.01
Al$_2$O$_3$	18.99	19.23	18.65	18.93	19.17	19.25	18.73	19.25	19.26	18.92	18.68	19.14
SiO$_2$	67.10	67.09	65.43	66.02	67.08	67.05	65.83	66.85	66.01	66.55	64.93	66.97
K$_2$O	10.61	9.25	14.30	11.59	9.49	9.32	11.29	9.90	10.76	11.02	13.81	10.14
CaO	0.00	0.03	0.07	0.03	0.32	0.00	0.00	0.02	0.06	0.02	0.00	0.07
FeO	0.03	0.06	0.04	0.00	0.19	0.22	0.10	0.10	0.02	0.03	0.09	0.05
MnO	0.06	0.02	0.00	0.02	0.01	0.01	0.00	0.01	0.04	0.02	0.01	0.00
BaO	0.20	0.60	0.59	0.53	0.59	0.64	0.40	0.13	0.77	0.23	0.98	0.24
Total	97.05	96.35	99.39	97.23	96.89	96.61	96.40	96.34	97.18	96.90	98.78	96.81
Structural formulae based on 8 atoms of oxygen												
Na	0.01	0.00	0.02	0.01	0.00	0.01	0.00	0.00	0.02	0.01	0.02	0.02
Al	1.02	1.04	1.01	1.03	1.03	1.04	1.03	1.04	1.05	1.03	1.02	1.03
Si	3.07	3.08	3.02	3.05	3.07	3.07	3.06	3.07	3.04	3.06	3.01	3.07
K	0.62	0.54	0.84	0.68	0.55	0.55	0.67	0.58	0.63	0.65	0.82	0.59
Ba	0.00	0.01	0.01	0.01	0.01	0.01	0.01	0.00	0.01	0.00	0.02	0.00
K + Na + Ba	0.63	0.56	0.88	0.70	0.57	0.56	0.68	0.58	0.67	0.66	0.86	0.61
Al + Si	4.10	4.12	4.03	4.08	4.10	4.11	4.08	4.11	4.09	4.09	4.03	4.10

Group	Ba-poor K-feldspar										
Sample	WN-42		WN-33		WN-24			WN-16			
Na$_2$O	0.09	0.15	0.12	0.10	0.09	0.10	0.24	0.45	0.16	0.22	0.20
MgO	0.04	0.00	0.02	0.02	0.02	0.01	0.02	0.00		0.02	0.02
Al$_2$O$_3$	18.64	18.56	19.27	18.68	19.00	18.97	19.05	18.97	18.62	18.36	18.66
SiO$_2$	66.17	66.55	66.67	65.63	67.41	66.29	66.48	66.75	65.25	64.36	64.92
K$_2$O	12.90	11.68	9.50	12.77	10.02	11.59	11.14	10.57	14.88	16.09	15.89
CaO	0.02	0.02	0.04	0.01	0.00	0.03	0.00	0.01	0.06	0.04	0.12
FeO	0.11	0.08	0.02	0.03	0.13	0.00	0.11	0.14	0.04	0.05	0.02
MnO	0.03	0.00	0.03	0.01	0.02	0.02	0.01	0.00	0.02	0.00	0.00
BaO	0.15	0.31	0.72	0.68	0.12	0.46	0.39	0.57	0.13	0.10	0.51
Total	98.14	97.35	96.38	97.93	96.81	97.47	97.44	97.47	99.16	99.24	100.34
Structural formulae based on 8 atoms of oxygen											
Na	0.01	0.01	0.01	0.01	0.01	0.01	0.02	0.04	0.01	0.02	0.02
Al	1.01	1.01	1.04	1.02	1.02	1.03	1.03	1.03	1.01	1.01	1.01
Si	3.05	3.07	3.07	3.04	3.08	3.05	3.05	3.06	3.01	3.00	2.99
K	0.76	0.69	0.56	0.75	0.58	0.68	0.65	0.62	0.88	0.96	0.93
Ba	0.00	0.01	0.01	0.01	0.00	0.01	0.01	0.01	0.00	0.00	0.01
K + Na + Ba	0.77	0.71	0.58	0.78	0.59	0.70	0.68	0.67	0.89	0.98	0.96
Al + Si	4.06	4.07	4.11	4.06	4.10	4.08	4.08	4.08	4.03	4.00	4.01

(continued)

TABLE 1. (*contd*.)

Group	Ba-rich K feldspar											
Sample	WN-2-28		WN-2-25									WN-2-24
Na$_2$O	0.17	0.19	0.14	0.09	0.21	0.15	0.10	0.20	0.10	0.15	0.17	0.13
MgO	0.00	0.01	0.00	0.02	0.01	0.02	0.00	0.03	0.01	0.00	0.02	0.03
Al$_2$O$_3$	19.13	19.04	19.74	19.43	20.07	19.85	19.61	20.66	20.84	20.56	20.39	19.84
SiO$_2$	66.42	65.71	64.27	62.60	63.06	65.15	64.55	58.79	58.46	59.52	61.29	64.44
K$_2$O	9.01	8.97	9.07	9.63	8.81	9.01	8.56	8.54	8.76	9.11	8.68	9.15
CaO	0.00	0.00	0.00	0.00	0.00	0.00	0.00	0.01	0.00	0.00	0.00	0.00
FeO	0.02	0.02	0.04	0.02	0.08	0.01	0.07	0.00	0.01	0.02	0.03	0.02
MnO	0.00	0.00	0.01	0.00	0.00	0.03	0.00	0.01	0.02	0.01	0.01	0.00
BaO	1.36	2.45	2.95	4.89	4.65	3.43	3.18	8.68	9.08	8.23	6.86	3.66
Total	96.11	96.39	96.21	96.68	96.89	97.65	96.08	96.92	97.28	97.60	97.46	97.26
Structural formulae based on 8 atoms of oxygen												
Na	0.02	0.02	0.01	0.01	0.02	0.01	0.01	0.02	0.01	0.01	0.02	0.01
Al	1.04	1.04	1.09	1.09	1.12	1.08	1.08	1.19	1.21	1.18	1.15	1.09
Si	3.07	3.06	3.01	2.99	2.98	3.02	3.03	2.88	2.87	2.89	2.93	3.01
K	0.53	0.53	0.54	0.59	0.53	0.53	0.51	0.53	0.55	0.56	0.53	0.54
Ba	0.02	0.04	0.05	0.09	0.09	0.06	0.06	0.17	0.17	0.16	0.13	0.07
K + Na + Ba	0.57	0.59	0.61	0.69	0.64	0.61	0.58	0.72	0.73	0.74	0.67	0.62
Al + Si	4.11	4.10	4.11	4.08	4.10	4.10	4.11	4.08	4.07	4.07	4.09	4.10

Group	Ba-rich K feldspar											
Sample	WN-2-17			WN-44							WN-37	WN-33
Na$_2$O	0.15	0.19	0.21	0.21	0.18	0.05	0.09	0.18	0.15	0.25	0.28	0.26
MgO	0.02	0.00	0.00	0.01	0.02	0.02	0.02	0.04	0.02	0.00	0.02	0.01
Al$_2$O$_3$	19.85	20.12	21.02	20.21	19.95	20.56	20.50	20.19	20.34	20.43	21.10	21.37
SiO$_2$	65.15	62.32	58.38	62.01	64.06	61.75	61.44	61.61	61.51	61.43	58.17	55.27
K$_2$O	9.01	8.60	8.16	8.77	7.99	7.58	7.75	8.39	8.22	7.34	7.19	8.93
CaO	0.00	0.02	0.01	0.01	0.02	0.00	0.00	0.02	0.01	0.02	0.00	0.02
FeO	0.01	0.00	0.01	0.00	0.00	0.00	0.00	0.01	0.00		0.00	0.00
MnO	0.03	0.00	0.00	0.03	0.00	0.00	0.04	0.00	0.02	0.03	0.01	0.01
BaO	3.43	5.63	10.02	5.82	4.31	6.67	6.99	6.35	6.64	7.27	10.54	12.36
Total	97.65	96.88	97.81	97.06	96.53	96.63	96.82	96.79	96.91	96.76	97.31	98.23
Structural formulae based on 8 atoms of oxygen												
Na	0.01	0.02	0.02	0.02	0.02	0.00	0.01	0.02	0.01	0.02	0.03	0.03
Al	1.08	1.13	1.21	1.13	1.10	1.16	1.16	1.14	1.15	1.15	1.22	1.27
Si	3.02	2.97	2.86	2.96	3.01	2.95	2.94	2.95	2.95	2.95	2.86	2.78
K	0.53	0.52	0.51	0.53	0.48	0.46	0.47	0.51	0.50	0.45	0.45	0.57
Ba	0.06	0.10	0.19	0.11	0.08	0.12	0.13	0.12	0.12	0.14	0.20	0.24
K + Na + Ba	0.61	0.64	0.72	0.66	0.57	0.59	0.61	0.65	0.64	0.61	0.68	0.84
Al + Si	4.10	4.09	4.07	4.09	4.11	4.11	4.10	4.09	4.09	4.10	4.08	4.04

(continued)

T ABLE 1. (*contd*.)

Group	Ba-rich K feldspar									
Sample	WN-33		WN-24				WN-22	WN-16		
Na$_2$O	0.31	0.23	0.20	0.27	0.22	0.18	0.20	0.17	0.24	0.26
MgO	0.00	0.02	0.00	0.01	0.00	0.03	0.01	0.00	0.02	0.01
Al$_2$O$_3$	21.48	21.34	22.23	22.72	22.44	21.65	21.24	21.94	21.06	21.70
SiO$_2$	55.55	56.46	53.14	51.89	52.08	56.34	58.34	52.69	58.89	55.01
K$_2$O	8.28	8.81	6.00	5.97	5.75	6.40	6.88	7.40	6.47	6.53
CaO	0.01	0.03	0.01	0.01	0.00	0.05	0.00	0.01	0.00	0.01
FeO	0.04	0.01	0.01	0.00	0.02	0.00	0.01	0.00	0.03	0.03
MnO	0.00	0.02	0.02	0.03	0.01	0.02	0.00	0.03	0.03	0.02
BaO	12.46	11.54	16.17	17.85	17.44	12.18	10.78	15.57	10.48	14.05
Total	98.13	98.46	97.78	98.76	97.95	96.84	97.46	97.80	97.23	97.61
Structural formulae based on 8 atoms of oxygen										
Na	0.03	0.02	0.02	0.03	0.02	0.02	0.02	0.02	0.02	0.03
Al	1.27	1.25	1.34	1.38	1.37	1.28	1.23	1.33	1.21	1.29
Si	2.78	2.80	2.73	2.68	2.70	2.82	2.86	2.72	2.88	2.78
K	0.53	0.56	0.39	0.39	0.38	0.41	0.43	0.49	0.40	0.42
Ba	0.24	0.22	0.32	0.36	0.35	0.24	0.21	0.31	0.20	0.28
K + Na + Ba	0.80	0.80	0.74	0.78	0.76	0.66	0.66	0.82	0.63	0.72
Al + Si	4.05	4.05	4.07	4.06	4.06	4.09	4.09	4.05	4.09	4.07

Group	Ba-rich K feldspar									
Sample	WN-16	WN-15		WN-14	WN-13			WN-10	WN-5	
Na$_2$O	0.13	0.19	0.25	0.27	0.18	0.29	0.33	0.35	0.22	0.19	0.29
MgO	0.02	0.02	0.00	0.00	0.00	0.02	0.01	0.00	0.06	0.03	0.00
Al$_2$O$_3$	21.20	22.39	23.13	22.34	22.76	22.18	22.97	21.50	21.35	21.76	22.96
SiO$_2$	55.08	52.07	49.03	52.20	50.42	52.37	49.20	56.26	56.86	55.53	49.14
K$_2$O	6.19	5.70	6.13	6.27	5.43	6.24	6.12	6.76	7.42	7.61	6.12
CaO	0.02	0.00	0.01	0.03	0.01	0.02	0.00	0.00	0.02	0.05	0.04
FeO	0.00	0.02	0.00	0.01	0.03	0.00	0.03	0.03	0.00	0.00	0.02
MnO	0.00	0.02	0.04	0.02	0.01	0.01	0.01	0.00	0.04	0.02	0.01
BaO	14.18	17.37	20.51	17.28	19.46	17.07	20.26	12.77	11.89	13.26	20.36
Total	96.82	97.78	99.10	98.42	98.30	98.19	98.93	97.67	97.86	98.44	98.94
Structural formulae based on 8 atoms of oxygen											
Na	0.01	0.02	0.03	0.03	0.02	0.03	0.03	0.03	0.02	0.02	0.03
Al	1.27	1.37	1.44	1.36	1.41	1.35	1.43	1.27	1.25	1.28	1.43
Si	2.80	2.70	2.59	2.69	2.65	2.70	2.60	2.81	2.82	2.78	2.60
K	0.40	0.38	0.41	0.41	0.36	0.41	0.41	0.43	0.47	0.49	0.41
Ba	0.28	0.35	0.43	0.35	0.40	0.35	0.42	0.25	0.23	0.26	0.42
K + Na + Ba	0.70	0.75	0.86	0.79	0.78	0.79	0.87	0.71	0.72	0.76	0.87
Al + Si	4.07	4.07	4.04	4.05	4.06	4.05	4.04	4.07	4.07	4.06	4.03

(continued)

TABLE 1. (*contd.*)

Group	Cymrite									
Sample	WN-15				WN-13					
Na₂O	0.10	0.09	0.18	0.08	0.27	0.17	0.19	0.13	0.21	0.09
MgO	0.03	0.02	0.00	0.01	0.00	0.00	0.06	0.02	0.00	0.02
Al₂O₃	25.99	25.55	25.96	25.31	25.19	25.90	25.67	25.46	25.58	25.73
SiO₂	31.17	31.39	31.19	31.27	32.74	31.65	31.82	32.73	32.15	32.04
K₂O	0.18	0.15	0.18	0.22	0.34	0.19	0.12	0.49	0.33	0.26
CaO	0.01	0.03	0.02	0.00	0.02	0.01	0.02	0.01	0.02	0.00
FeO	0.00	0.01	0.03	0.05	0.00	0.04	0.00	0.00	0.01	0.00
MnO	0.01	0.00	0.00	0.01	0.01	0.00	0.01	0.04	0.03	0.02
BaO	38.21	38.08	38.07	38.31	36.40	37.71	37.66	36.35	36.84	37.46
Total	95.70	95.32	95.63	95.26	94.97	95.67	95.55	95.23	95.17	95.62
Structural formulae based on 8 atoms of oxygen										
Na	0.01	0.01	0.02	0.01	0.03	0.02	0.02	0.02	0.03	0.01
Al	1.98	1.96	1.98	1.95	1.90	1.97	1.95	1.92	1.94	1.95
Si	2.02	2.04	2.02	2.04	2.10	2.04	2.05	2.09	2.07	2.06
K	0.01	0.01	0.01	0.02	0.03	0.02	0.01	0.04	0.03	0.02
Ba	0.97	0.97	0.97	0.98	0.91	0.95	0.95	0.91	0.93	0.94
K + Na + Ba	1.00	0.99	1.00	1.01	0.98	0.99	0.98	0.97	0.98	0.98
Al + Si	4.00	4.00	4.00	3.99	4.00	4.01	4.00	4.01	4.01	4.01

36.35–38.31 wt.%, 31.17–32.74 wt.% and 25.19–25.99 wt.%, respectively. The K_2O and Na_2O contents of the cymrite fall within the limited ranges of 0.12–0.49 wt.% and 0.09–0.27 wt.%, respectively. The BaO and SiO_2 contents of the cymrites, and their correlations, are similar to those reported in previous studies (Fig. 8*a*) (Reinecke, 1982; Jakobsen, 1990; Moro *et al.*, 2001).

Formulae calculations indicate that the cymrites are stoichiometric in composition (Table 1). As shown in Fig. 8*b–c*, the correlations of $(K + Na)_{apfu}$–Si_{apfu} and Ba_{apfu}–Si_{apfu} are close to the theoretical ones, and comparable to those reported previously (Reinecke, 1982; Jakobsen, 1990; Moro *et al.*, 2001).

Causes of the non-stoichiometry

As discussed above, the Ba-poor K-feldspars and Ba-rich K-feldspars in our samples are non-stoichiometric. Normally, non-stoichiometry can be caused by analytical errors or the presence of monovalent or bivalent cations not included in the EMP analyses (Orberger *et al.*, 2005). The strong linear correlations of K_2O–SiO_2 in the Ba-poor K-feldspars (Fig. 4*a*) and BaO–SiO_2 in the Ba-rich K-feldspars (Fig. 6*b*) argue against the possibility of significant analytical errors in the microprobe

analyses of K, Ba, Al and Si. We suggest, therefore, that some cations in the Ba-poor K-feldspars and Ba-rich K-feldspars might not have been included in the microprobe analyses, thus accounting for the non-stoichiometry.

In addition to Na^+, K^+, Ca^{2+} and Ba^{2+}, other monovalent or bivalent cations such as Li^+, NH_4^+, Rb^+ and Sr^{2+} can occupy the M site in feldspars (Smith and Brown, 1988). Ba-rich K-feldspars with high contents of NH_4^+ (corresponding to as much as 56 mol.% buddingtonite) have been reported from mineralized Devonian black shales in the Selwyn Basin, Northwest Territories, Canada, for which it was suggested the NH_4^+ originated from the decomposition of intraformational organic matter (Orberger *et al.*, 2005). As shown in Fig. 6, our samples of Ba-rich K-feldspar and those studied by Orberger *et al.* (2005) have similar compositional characteristics, including elemental correlations and non-stoichiometric features. Furthermore, the mudstones of the Hetang Formation are also rich in organic matter, with TOC contents of 2.10 to 27.13 wt.% (Chang *et al.*, 2016). These strong similarities indicate that the main cause of non-stoichiometry in our samples might be NH_4^+, and to pursue this further, sample WN-24 was analysed by Raman and IR spectroscopy. It contains large aggregates of Ba-rich K-feldspar favourable for spectroscopic analysis (Fig. 5*c*).
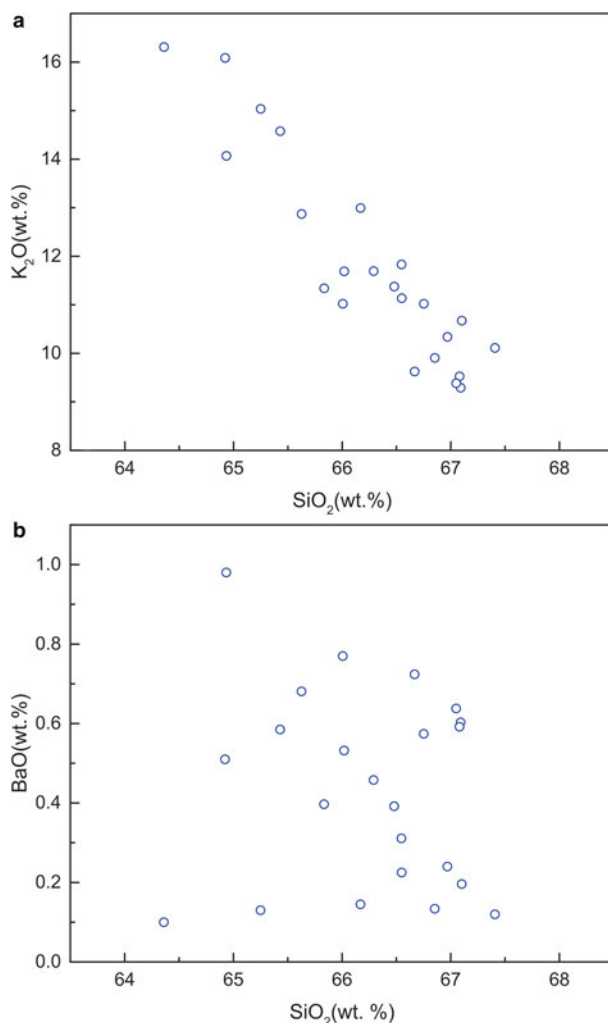
10

FIG. 4. Plots of the contents of main components in Ba-poor K-feldspar: (*a*) K$_2$O and SiO$_2$, a strong negative linear correlation between K$_2$O and SiO$_2$ is observed; (*b*) BaO and SiO$_2$, only a very weak negative correlation between BaO and SiO$_2$ can be recognized.

The Raman spectra for the Ba-rich K-feldspar aggregates in sample WN-24 are presented in Fig. 9. The 100–1200 cm^{-1} region of the spectra is characterized by peaks typical of K-feldspar (Freeman *et al.*, 2008). The strongest peak around 513 cm^{-1} and other peaks in the 450–520 cm^{-1} region (e.g. the peak around 472 cm^{-1}) belong to the ring-breathing modes of the four-membered rings of the tetrahedra. The peaks around 157 and 283 cm^{-1} correspond to the rotation–transaction mode of four-membered rings and the cage-shear mode, respectively.

In addition, the weak peaks around 807 and 1112 cm^{-1} can be assigned to the deformation and vibrational stretching modes of the tetrahedra, respectively.

The 1400–4000 cm^{-1} region on the spectra includes a broad peak between 2800 and 3000 cm^{-1}, and three other peaks around 1463, 1609 and 3068 cm^{-1}. The broad peak between 2800 and 3000 cm^{-1} was also observed on the Raman spectra of tetra-n-butyl ammonium fluoride semi-clathrate hydrate, and it was attributed to the O–H vibration of the hydration water (Sakamoto *et al.*,
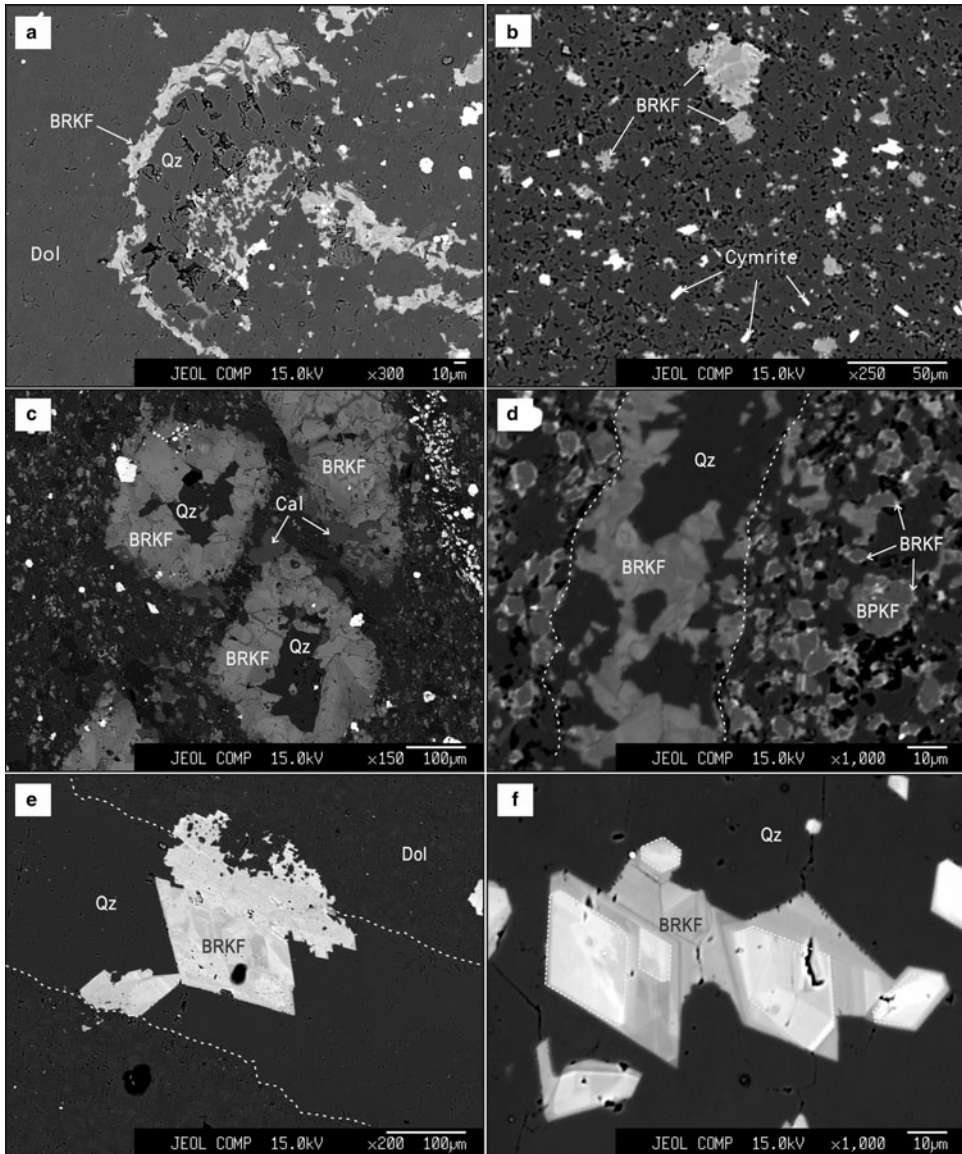
11

FIG. 5. BSE images showing the occurrences of Ba-rich K-feldspars (BRKF): (*a*) Ba-rich K-feldspars occur as fillings of voids in dolostone, accompanied by quartz, Sample WN-8; (*b*) Ba-rich K-feldspars and cymrite crystals occur as dispersive grains in chert, Sample WN-13; (*c*) Ba-rich K-feldspars occur as rectangular and rhombic aggregates, accompanied by sporadic calcite and quartz occurs in some of the aggregates, Sample WN-24; (*d*) Ba-rich K-feldspar-bearing veins in mudstone, the veins are mainly composed of Ba-rich K-feldspar and quartz, the Ba-rich K-feldspars occur as amorphous aggregates consisting of anhedral to subhedral small Ba-rich K-feldspar grains, and the Ba-rich K-feldspars in veins are associated with those (rims) in the matrix, Sample WN-42; (*e*) Ba-rich K-feldspar-bearing veins in dolostone, the veins are mainly composed of Ba-rich K-feldspar and quartz, some Ba-rich K-feldspars occur as euhedral rhombic grains, and the Ba-rich K-feldspars in veins are associated with those Ba-rich K-feldspar fillings in the matrix, WN-5; (*f*) euhedral Ba-rich K-feldspar grains in veins observed in mudstone, the euhedral Ba-rich K-feldspar grains are surrounded by or connected with Ba-rich K-feldspars with lower BaO contents, Sample WN-2-25. Mineral abbreviations: Qz = quartz, Cal = calcite, Dol = dolomite (Whitney and Evans, 2010).
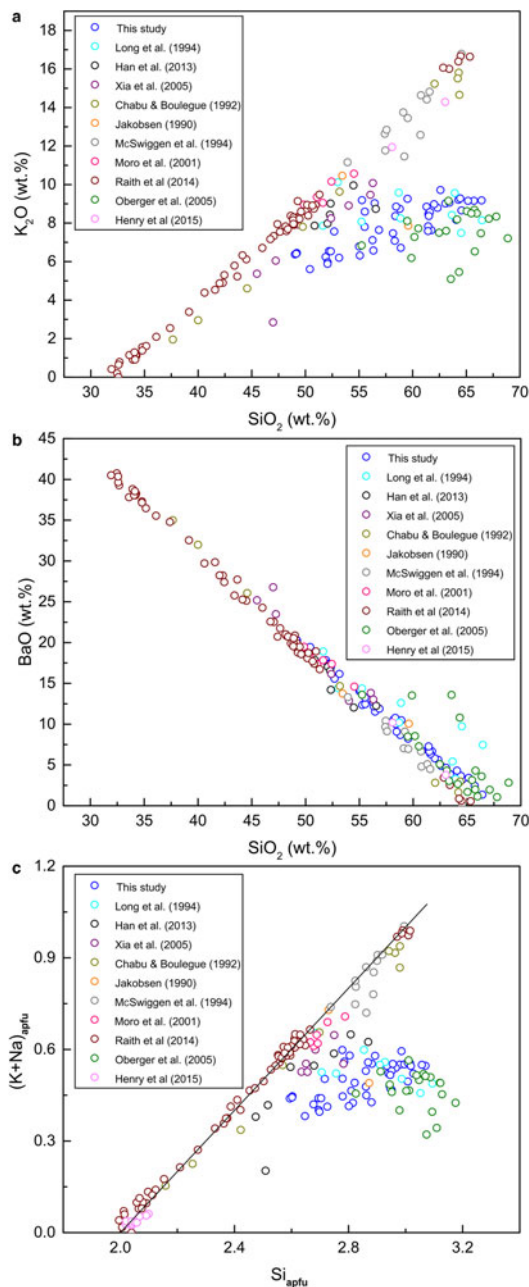
FIG. 6. Plots of the contents of main components in Ba-rich K-feldspars in this and previous studies: (*a*) K$_2$O and SiO$_2$, the Ba-rich K-feldspars in most of the previous studies a strong negative linear correlation between K$_2$O and SiO$_2$ (Jakobsen, 1990; Chabu and Boulègue, 1992; McSwiggen *et al.*, 1994; Moro *et al.*, 2001; Xia *et al.*, 2005; Han *et al.*, 2013; Raith *et al.*, 2014; Henry *et al.*, 2015), whereas the data points from Long *et al.* (1994), Orberger *et al.* (2005), and this study are distributed sparsely in a single area away from the line; (*b*) BaO and SiO$_2$, the Ba-rich K-feldspars of this study show a similar negative linear correlation between BaO and SiO$_2$, the Ba-rich K-feldspars of Long *et al.* (1994), Orberger *et al.* (2005) and this study show higher SiO$_2$ contents; (*c*) (K + Na)$_{apfu}$ and Si$_{apfu}$, similar correlation characteristics to (*a*) are observed, the black solid line represents the theoretical compositional assemblage of hyalophane.
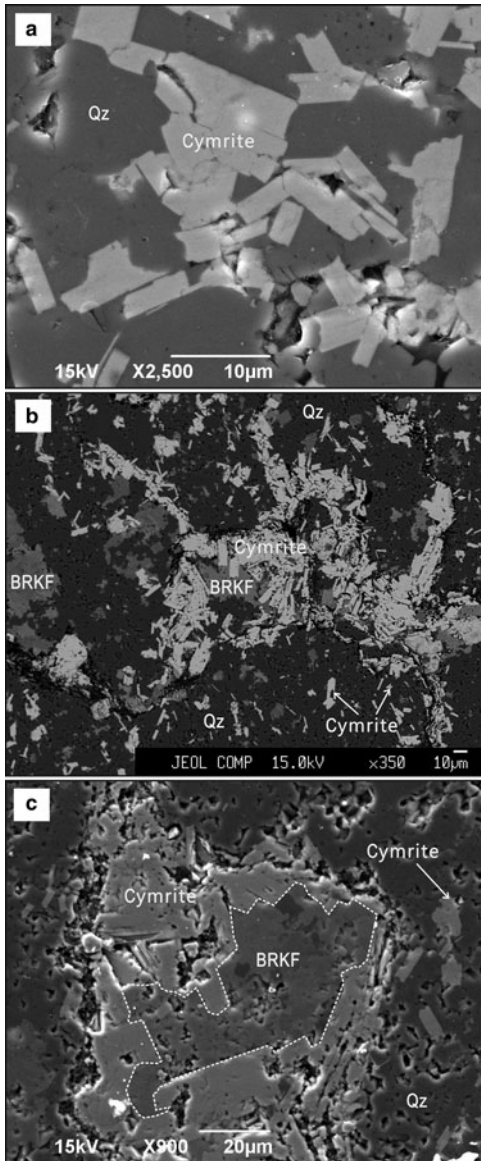
13

FIG. 7. BSE and SE images showing the occurrences of cymrites in chert: (*a*) cymrites occur as euhedral tabular crystals in voids in the matrix, Sample WN-13; (*b*) cymrite crystals and Ba-rich K-feldspars (BRKF) fill the microcracks, and occur as dispersed grains in the matrix, Sample WN-15; (*c*) cymrite crystals overgrowth on Ba-rich K-feldspar grains, Sample WN-15.

2008). In comparison, both the broad peak and the peak around 3068 cm^{-1} were observed in the Raman spectra of MgNH$_4$PO$_4$·6H$_2$O (Stefov *et al.*, 2005). The differences in the Raman spectra of the two minerals reveal the contribution of NH$_4^+$ to the 3068 cm^{-1} peak. Furthermore, the peaks around 1463 and 1609 cm^{-1} can be assigned, respectively to the v_4 mode of ammonium ions and δ(HOH) vibrations (Stefov *et al.*, 2005).

Additional evidence for the presence of NH$_4^+$ is provided by the IR spectra of the Ba-rich K-feldspar aggregates. As shown in Fig. 10, the strong peak near 1400 cm^{-1} and two other peaks around 3100 and 3300 cm^{-1} correspond to the N–H bending and N–H stretching vibrations of NH$_4^+$, respectively (Nyquist and Kagel, 1971; Boyd and Philippot, 1998). A peak near 3600 cm^{-1} is observed in all the IR spectra, accompanied by a peak around 3400 cm^{-1} in some spectra (Fig. 10), and these peaks correspond to the O–H stretching vibration mode of hydration water (Nyquist and Kagel, 1971). In contrast, the peak around 1600 cm^{-1} in some spectra can be attributed to the H–O–H bending motion mode of hydration water (Nyquist and Kagel, 1971).

In brief, the Raman and IR spectra of the Ba-rich K-feldspar aggregates show that NH$_4^+$ and hydration water are present in our samples of Ba-rich K-feldspar, and they probably indicate the presence of a buddingtonite (NH$_4$AlSi$_3$O$_8$·1/2H$_2$O) component in the Ba-rich K-feldspar (Smith and Brown, 1988; Orberger *et al.*, 2005). We suggest, therefore, that the occupancy of NH$_4^+$ on the *M* sites of the Ba-rich K-feldspars is the main cause of non-stoichiometry recorded by our EMP analyses. Moreover, although we did not carry out any direct spectroscopic measurements on the Ba-poor K-feldspars, it is reasonable to conclude that their non-stoichiometry might also be caused by the incorporation of NH$_4^+$, given the similar non-stoichiometric characteristics of the Ba-rich K-feldspars and Ba-poor K-feldspars (depleted K and excessive Al and Si; Table 1; Fig. 4*a*; Fig. 6*a* and *c*), and their textural relationships (Fig. 3). The mechanisms for incorporation of NH$_4^+$ into the feldspars are discussed below.

Formation mechanisms

Ba-rich K-feldspars

Two mechanisms have commonly been proposed for the formation of Ba-rich K-feldspars: (1) the replacement of authigenic barite; and (2) as an authigenic phase crystallizing from Ba–Al–Si gels (McSwiggen *et al.*, 1994; Moro *et al.*, 2001). The replacement of authigenic barite occurs during late diagenetic or metamorphic processes, with the
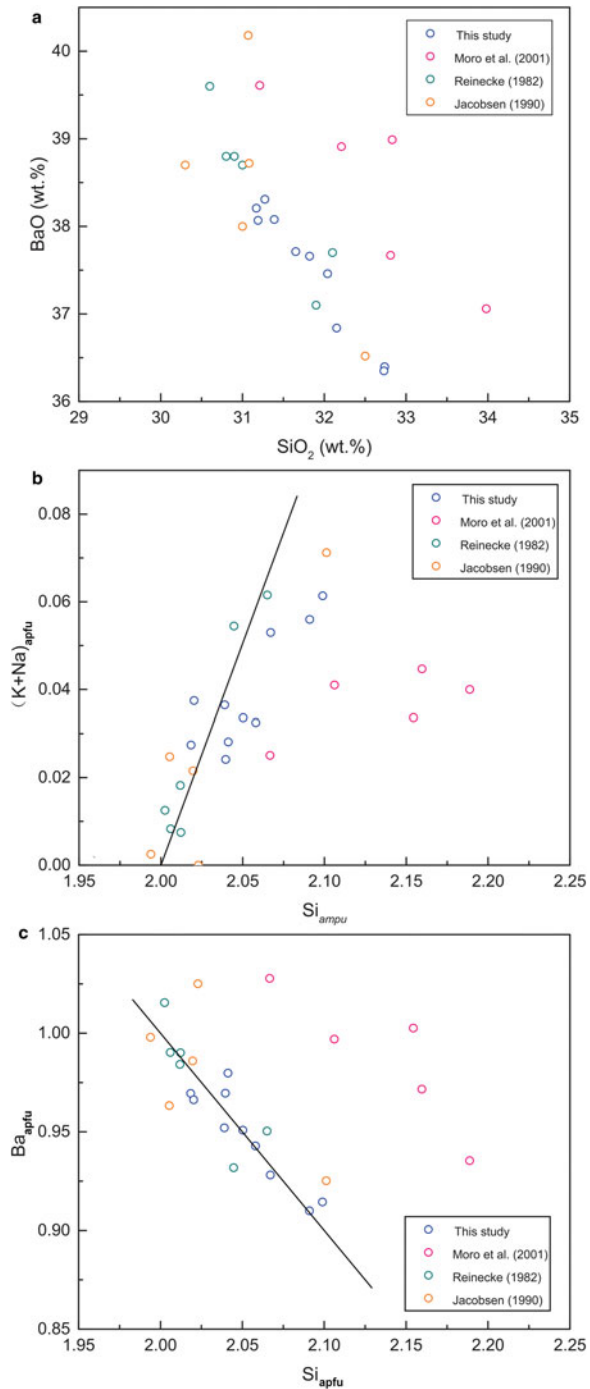
FIG. 8. Plots of the contents of main components in cymrites in this and previous studies: (*a*) BaO and SiO$_2$, a strong negative linear correlation similar to previous studies is observed; (*b*) (K + Na)$_{apfu}$ and Si$_{apfu}$; and (*c*) Ba$_{apfu}$ and Si$_{apfu}$, the data points are distributed closely along the theoretical line (black solid line) of cymrite, and strong linear correlations similar to previous studies are observed.
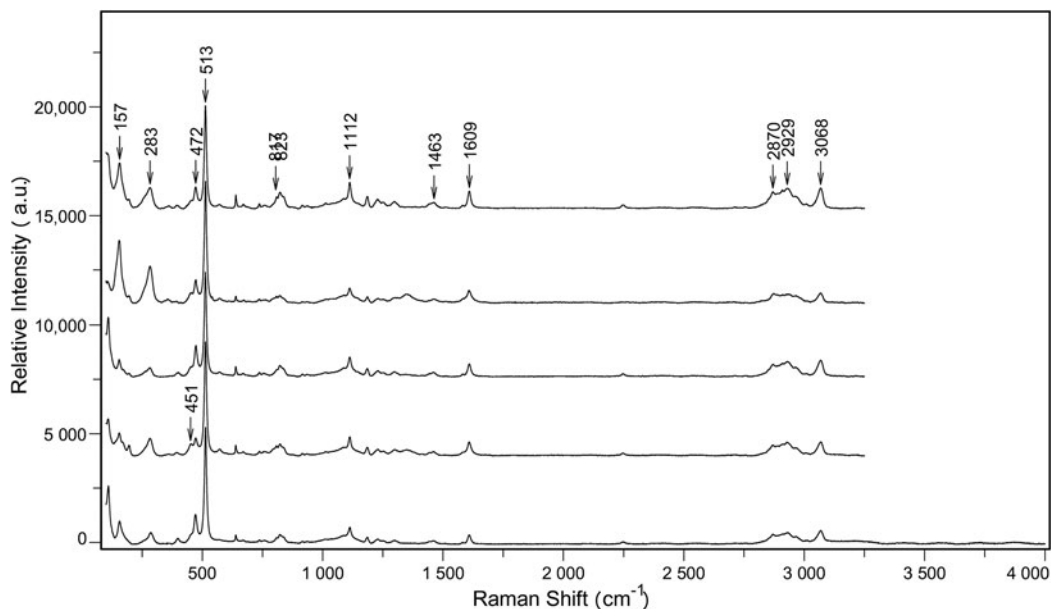
15

FIG. 9. Raman spectra of Ba-rich K-feldspars in Sample WN-24, typical peaks associated with K-feldspar, NH_4^+, and H_2O are observed in all the spectra and marked out in the figure.

baryte dissolved under a relatively reducing environment and the released barium precipitated as Ba-rich K-feldspar (Chabu and Boulègue, 1992; McSwiggen *et al.*, 1994). In our study we found no mineral relicts that would indicate the prior existence of authigenic baryte or textural evidence to support the replacement of baryte. We suggest, therefore, that baryte was not the precursor of the Ba-rich K-feldspar in our samples. The alternative mechanism of forming Ba-rich K-feldspars from hydrated Ba–Al–Si gels involves a late multi-stage diagenetic process that starts with hydrated Ba-silicates with higher contents of water (such as harmotome, $BaAl_2Si_6O_6\cdot6H_2O$), with dehydration reactions leading to the formation of cymrite and eventually celsian (Fortey and Beddoe–Stephens, 1982; Jakobsen, 1990; Raith *et al.*, 2014).

The formation of Ba–Al–Si gels is thought to be associated with hydrothermal activity (Coats *et al.*, 1980; Large, 1980; Fortey and Beddoe–Stephens, 1982; Russell *et al.*, 1984; Jakobsen, 1990; McSwiggen *et al.*, 1994; Moro *et al.*, 2001). Large amounts of Ba and SiO_2 could be released into seawater during exhalative hydrothermal activity and then precipitated on the seafloor as a silica gel under reducing conditions (Large, 1980). Ba-rich K-feldspar-bearing cherts have been reported by Fortey and Beddoe–Stephens (1982) and

Jakobsen (1990), who suggested that the Ba-rich K-feldspars were of exhalative hydrothermal origin. Similarly, the Ba-rich K-feldspars in our samples of chert could have originated from Ba–Al–Si gels that formed during exhalative hydrothermal activity. The dispersed nature of the grains of Ba-rich K-feldspar (Fig. 5*a*) and the reducing sedimentary environment of the chert are consistent with this mechanism of formation (Chang *et al.*, 2016).

In contrast, the cross-cutting Ba-rich K-feld-spar-bearing veins in the mudstones and dolos-tones demonstrate that the Ba-rich hydrothermal fluids also infiltrated the strata along cracks and formed Ba-Al-Si gels (Fig. 5*d–f*). Furthermore, on the basis of textural relationships we suggest that the hydrothermal fluids that formed the veins penetrated through voids into the matrix, leading to the formation of Ba-rich K-feldspar rims in the mudstones and Ba-rich K-feldspar void fillings in the dolostones (Fig. 5*d–e*). The infiltration of the hydrothermal fluids might have occurred when the sediments were relatively unconsolidated, so that the fluids could move easily through the inter-granular spaces of the sediments and form abundant micro-scale veins (Fig. 5*d–e*). Compositional zoning of the Ba-rich K-feldspar grains in the veins could be a result of heterogeneous crystallizing conditions (Fig. 5*e–f*), while
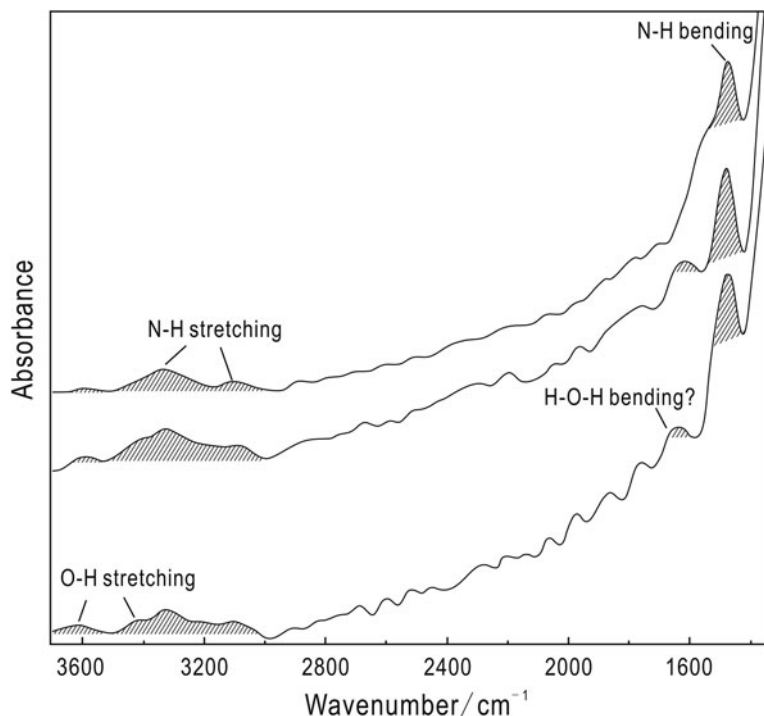
16

FIG. 10. Infrared spectra of Ba-rich K-feldspars in Sample WN-24, typical peaks corresponding to NH$_4^+$ and H$_2$O are observed in all the spectra.

the more intense zoning of the Ba-rich K-feldspar aggregates could be attributed to Ba-depleted Ba-rich K-feldspars forming overgrowths on early-formed Ba-enriched grains of Ba-rich K-feldspar (Fig. 5*f*).

In addition, the peculiar occurrence of the Ba-rich K-feldspar aggregates in sample WN-24 suggests a distinctive formation process. The regular shapes of the aggregates might have been inherited from crystallized precursor minerals, and the consistent occurrence of calcite around the aggregates suggests a genetic relationship (Fig. 5*c*). Consequently, we suggest tentatively that the regularly shaped aggregates were originally calcite or dolomite crystals. These crystals would have been dissolved easily by acidic and Ba-rich hydrothermal fluids, and Ba–Al–Si gels would then have been precipitated in the resulting voids. A small amount of Ca-enriched fluid might have been preserved, leading to the formation of the calcite around the aggregates.

In brief, we suggest the Ba-rich K-feldspars in our samples formed from Ba-rich hydrothermal fluids in multiple stages, and that the intensity of the

hydrothermal activity fluctuated during the various stages. The Ba-rich K-feldspar-bearing cherts were possibly formed when hydrothermal activity was intense, and when the hydrothermal fluids were transported to the seafloor. The sedimentary strata would have been infiltrated by the hydrothermal fluids as they ascended. At other stages, the hydrothermal activity might have been insufficiently intense enough to form bedded chert, and at times most of the hydrothermal fluids might simply have infiltrated the pile of sedimentary strata. The results of early-stage hydrothermal activity could have been overprinted by late-stage activity, which means that the Ba-rich K-feldspars in any one sample might have formed during multiple stages of hydrothermal activity.

The contrasting BaO contents of the Ba-rich K-feldspars in different samples might therefore be related to variable intensities of hydrothermal activity at different stages (Fig. 2). As shown in Fig. 2, the BaO contents of the Ba-rich K-feldspars are highest at the bottom of the Hetang Formation and decrease upwards to the calcareous mudstone layer, indicating that hydrothermal activity was

intense at the beginning of the Cambrian, but gradually weakened thereafter.

During the degradation of sedimentary deposits organic matter can form, which can then be dissolved in pore fluids; moreover, hydrothermal fluids can boost the formation of NH_4^+ from organic matter (Orberger *et al.*, 2005). Therefore, large amounts of NH_4^+ could have been derived from young organic-rich sedimentary strata such as the late Neoproterozoic Doushantuo Formation (Yang *et al.*, 2015) and the Hetang Formation, and then incorporated into hydrothermal fluids. The hydrothermal fluids would then have transported the NH_4^+ into voids in the sediments and contributed to the formation of the Ba-rich K-feldspars.

A multi-stage mechanism of formation is consistent with the tectonic setting of extension during the Ediacaran–Cambrian transition (Wang and Li, 2003). Multiple stages of hydrothermal fluids from a deep-seated heat source could have been driven upwards along faults under enhanced edge-driven convection during that period (Chen *et al.*, 2009). Except for the aforementioned baryte and vanadium deposits, polymetallic sulfide deposits of hydrothermal origin and various occurrences of chert associated with multi-episodic hydrothermal activities have also been reported previously (Steiner *et al.*, 2001; Jiang *et al.*, 2007; Chen *et al.*, 2009; Wang *et al.*, 2012), further supporting the idea that hydrothermal activities were prevalent in South China during the Ediacaran–Cambrian transition.

Ba-poor K-feldspars

In contrast to the Ba-rich K-feldspars, most Ba-poor K-feldspars in our samples occur independently of any Ba-bearing veins in the mudstones (Fig. 3 and Fig. 5*d*–*f*), and no Ba-poor K-feldspars have been observed in association with the Ba-rich K-feldspar aggregates in sample WN-24 (Fig. 5*c*). These observations suggest that the Ba-poor K-feldspars might not have formed directly from the hydrothermal fluids responsible for the Ba-rich K-feldspars. Rather, the presence of stoichiometric Ba-poor K-feldspars in sample WN-16 supports the idea that the Ba-poor K-feldspars were originally stoichiometric K-feldspars within the mudstone (Table 1). These K-feldspars might then have interacted with the infiltrating Ba-rich hydrothermal fluids, leading to the formation of the Ba-poor K-feldspars. However, as only small amounts of hydrothermal fluid could have infiltrated the sediments, the interactions between the K-feldspars and the hydrothermal fluids would have

been limited and incomplete. As a result, most of the Ba-poor K-feldspars still occur as normal grains rather than dissolved relics, and the core areas of some large K-feldspar grains have retained their original compositions (WN-16; Table 1).

During these interactions, Ba^{2+} and NH_4^+ in the hydrothermal fluids would have substituted for K^+ in the K-feldspars. The ionic radius of Ba^{2+} is 0.144 nm, similar to that of NH_4^+ (0.143 nm) (Honma and Itihara, 1981). The substitution of K^+ by Ba^{2+} occurs in the form of a coupled exchange between (K, Si) and (Ba, Al) (Gay and Roy, 1968), which requires a high activation energy and is obviously more difficult than substituting K^+ by NH_4^+ (Raith *et al.*, 2014). Therefore, relatively large amounts of K^+ might have been substituted by NH_4^+ during the interactions, while the substitution of K^+ by Ba^{2+} would have been more limited. As the SiO_2 content of buddingtonite is higher than that of K-feldspar, the SiO_2 content of Ba-poor K-feldspar will increase with the substitution of K^+ by NH_4^+, and this is consistent with the obvious negative correlation between SiO_2 and K_2O in the Ba-poor K-feldspars (Fig. 4*a*). In contrast, a decrease in SiO_2 content accompanies the substitution of K^+ by Ba^{2+}, as celsian has a lower SiO_2 content than K-feldspar. This process would be expected to produce a negative correlation between the SiO_2 and BaO contents of the Ba-poor K-feldspars. However, as the substitution of K^+ by Ba^{2+} is much weaker than that by NH_4^+, the negative correlation would be obscured by the changes in SiO_2 content caused by the substitution of K^+ by NH_4^+, and this explains why only a weak negative trend can be recognized on the BaO–SiO_2 plot (Fig. 4*b*).

Cymrite

Cymrite, $BaAl_2Si_2O_8 \cdot nH_2O$, where $n = 0.5$–1.0 (Back *et al.*, 2008), is a hydrated silicate mineral rarely found in nature (e.g. Hsu, 1994; Moro *et al.*, 2001). Its occurrence is usually associated with metasedimentary or hydrothermal ore deposits, as well as late-stage low-grade metamorphism (Matsubara and Kato, 1991; Hsu, 1994; Moro *et al.*, 2001; Sorokhtina *et al.*, 2008). It crystallize under hydrothermal conditions corresponding to a low-grade dynamothermal metamorphism, and develops as crystals in rock cavities (Matsubara and Kato, 1991; Hsu, 1994; Moro *et al.*, 2001; Sorokhtina *et al.*, 2008).

In our samples, the cymrite occurs as tabular crystals that are dispersed in the intergranular voids or micro-cracks of chert (Fig. 5*a* and Fig. 7), and this occurrence suggests it formed as a result of hydrothermal activity (Sorokhtina *et al.*, 2008),

consistent with the mechanism of formation proposed for the Ba-rich K-feldspars in the chert (see the section 'Formation mechanisms'). However, thin section observations and EMP analyses have shown that metamorphic minerals such as chlorite or muscovite are absent from our samples, indicating a lack of any significant regional metamorphism (Bucher and Grapes, 2011). Therefore, the presence of cymrite in our samples demonstrates that it can be stable under very low P–T (sub-metamorphic) conditions (Graham *et al.*, 1992; Hsu, 1994). Moreover, no celsian has been detected in the cymrite-bearing cherts, possibly because the dehydration of cymrite requires higher P–T conditions.

Micro-cracks would have assisted in the transportation and accumulation of Ba-rich fluids, where abundant cymrite and Ba-rich K-feldspars were formed (Fig. 7*b*). BaAl$_2$Si$_2$O$_8$·4H$_2$O is believed to be the precursor mineral of cymrite (Jakobsen, 1990), and the occurrence of both Ba-rich K-feldspar and BaAl$_2$Si$_2$O$_8$·4H$_2$O in unmetamorphosed rocks of the Navarana Fjord area, North Greenland, demonstrates that the formation of Ba-rich K-feldspar can precede the formation of cymrite under very low P–T conditions. This explains the overgrowth of cymrite on the Ba-rich K-feldspar, as shown in Fig. 7*c*.

Conclusions

Barium-rich silicates in the black shale sequence of the Hetang Formation, Anhui Province, South China, include Ba-poor K-feldspar, Ba-rich K-feldspar and cymrite. The Ba-poor K-feldspars have BaO contents that are <1.00 wt.%, and occur as grains in mudstone. The BaO contents of the Ba-rich K-feldspars are much higher, ranging from 1.36 to 20.51 wt.%. The Ba-rich K-feldspars occur mainly as rims around Ba-poor K-feldspar grains in mudstone, as void fillings in dolostone, and as dispersed grains in chert. Veins composed of Ba-rich K-feldspar and quartz are common in the mudstone and dolostone. The Ba-poor K-feldspars and Ba-rich K-feldspars have non-stoichiometric compositions, and EMP analyses yield compositions that total <100 wt.%. We suggest this is due to the incorporation of NH$_4^+$ and H$_2$O into the feldspars, based on the results of Raman and IR spectroscopy. The cymrite in our samples occurs as tabular crystals that are dispersed in chert, and it has compositions that are comparable to those reported in the literature (Reinecke, 1982; Jakobsen, 1990; Moro *et al.*, 2001).

We suggest that the formation of the Ba-silicates in our samples was related to multiple episodes of hydrothermal activity. The Ba-poor K-feldspars probably formed through interactions between pre-existing K-feldspars and Ba-rich hydrothermal fluids. The Ba-rich K-feldspars in the mudstones and dolostones might have formed mainly as a result of the infiltration of Ba-rich hydrothermal fluids into the sediments when they were still poorly consolidated. The Ba-rich K-feldspars and the cymrite in the cherts might have formed during diagenesis from Ba–Al–Si gels of exhalative hydrothermal origin. These proposed mechanisms of formation are consistent with a tectonic setting of extension in South China during the Ediacaran–Cambrian transition (Wang and Li, 2003; Chen *et al.*, 2009).

Acknowledgements

References

Back, M.E., Mandarino, J.A. and Fleischer, M. (2008) *Fleischer's Glossary of Mineral Species*, Mineralogical Record Incorporated, USA.

Boyd, S.R. and Philippot, P. (1998) Precambrian ammonium biogeochemistry: a study of the Moine metasediments, Scotland. *Chemical Geology*, **144**, 257–268.

Bucher, K. and Grapes, R. (2011) *Petrogenesis of Metamorphic Rocks*, Springer Berlin Heidelberg.

Chabu, M. and Boulegue, J. (1992) Barian feldspar and muscovite from the Kipushi Zn–Pb–Cu deposit, Shaba, Zaire. *Canadian Mineralogist*, **30**, 1143–1152.

Chang, C., Hu, W.X., Fu, Q., Cao, J., Wang, X.L. and Yao, S.P. (2016) Characterization of trace elements and carbon isotopes across the Ediacaran-Cambrian boundary in Anhui Province, South China: Implications for stratigraphy and paleoenvironment reconstruction. *Journal of Asian Earth Sciences*, **125**, 58–70.

Chen, D.Z., Wang, J.G., Qing, H.R., Yan, D.T. and Li, R.W. (2009) Hydrothermal venting activities in the Early Cambrian, South China: Petrological,

geochronological and stable isotopic constraints. *Chemical Geology*, **258**, 168–181.

Coats, J., Smith, C., Fortey, N., Gallagher, M., May, F. and McCourt, W. (1980) Strata-bound barium–zinc mineralization in Dalradian schist near Aberfeldy, Scotland. *Transactions of the Institution of Mining and Metallurgy Section B-Applied Earth Science*, **89**, B110–B122.

Deer, W.A., Howie, R.A. and Zussman, J. (2001) *Rock-Forming Minerals, Volume 4A: Framework Silicates*. The Geological Society, London, England.

Essene, E.J., Claflin, C.L., Giorgetti, G., Mata, P.M., Peacor, D.R., Arkai, P. and Rathmell, M.A. (2005) Two-, three- and four-feldspar assemblages with hyalophane and celsian: implications for phase equilibria in $BaAl_2Si_2O_8–CaAl_2Si_2O_8–NaAlSi_3O_8–KAIS_3O_8$. *European Journal of Mineralogy*, **17**, 515–535.

Fortey, N.J. and Beddoestephens, B. (1982) Barium silicates in stratabound Ba–Zn mineralization in the Scottish Dalradian. *Mineralogical Magazine*, **46**, 63–72.

Freeman, J.J., Wang, A., Kuebler, K.E., Jolliff, B.L. and Haskin, L.A. (2008) Characterization of natural feldspars by Raman spectroscopy for future planetary exploration. *Canadian Mineralogist*, **46**, 1477–1500.

Gay, P. and Roy, N.N. (1968) The mineralogy of the potassium-barium feldspar series III: Subsolidus relationships. *Mineralogical Magazine*, **36**, 914–932.

Graham, C.M., Tareen, J.A.K., Mcmillan, P.F. and Lowe, B.M. (1992) An experimental and thermyodynamic study of cymrite and celsian stability in the system $BaO–Al_2O_3–SiO_2–H_2O$. *European Journal of Mineralogy*, **4**, 251–269.

Han, S., Hu, K. and Cao, J. (2013) First discovery of zoned hyalophane in the barite deposits hosted in Early Cambrian black shales of South China and its geological implications. *Geological Review*, **59**, 1143–1149.

Henry, D.J., Will, C.N. and Mueller, P.A. (2015) Ba-rich K-feldspar from mafic xenoliths within Mesoarchean granitic rocks, Beartooth Mountains, Montana, USA: Indicators for barium metasomatism. *Canadian Mineralogist*, **53**, 185–198.

Honma, H. and Itihara, Y. (1981) Distribution of ammonium in minerals of metamorphic and granitic-rocks. *Geochimica et Cosmochimica Acta*, **45**, 983–988.

Hsu, L.C. (1994) Cymrite: new occurrence and stability. *Contributions to Mineralogy and Petrology*, **118**, 314–320.

Jakobsen, U.H. (1990) A hydrated barium silicate in unmetamorphosed sedimentary-rocks of Central North Greenland. *Mineralogical Magazine*, **54**, 81–89.

Jiang, S.Y., Yang, J.H., Ling, H.F., Chen, Y.Q., Feng, H.Z., Zhao, K.D. and Ni, P. (2007) Extreme enrichment of polymetallic Ni–Mo–PGE–Au in lower Cambrian black shales of South China: An Os isotope and PGE geochernical investigation. *Palaeogeography Palaeoclimatology Palaeoecology*, **254**, 217–228.

Large, D. (1980) Geological parameters associated with sediment-hosted, submarine exhalative Pb–Zn deposits: an empirical model for mineral exploration. *Geologisches Jahrbuch,* **D40**, 59–129.

Long, H., Long, J., Zhong, Y., Zhuang, S. and Liu, T. (1994) Discovery of hyalophane from the Vanadium deposit in the black rock series at Zhangcun–Zhengfang: Evidence for hydrothermal sedimentary origin. *Chinese Science Bulletin*, **39**, 636–638 [in Chinese].

Matsubara, S. and Kato, A. (1991) Edingtonite from the Shiromaru mine, Tokyo, Japan. *Ganko*, **86**, 273–277.

McSwiggen, P.L., Morey, G.B. and Cleland, J.M. (1994) Occurrence and genetic-implications of hyalophane in manganese-rich iron-formation, Cuyuna-Iron-Range, Minnesota, USA. *Mineralogical Magazine*, **58**, 387–399.

Moro, M.C., Cembranos, M.L. and Fernandez, A. (2001) Celsian, (Ba,K)-feldspar and cymrite from sedex barite deposits of Zamora, Spain. *Canadian Mineralogist*, **39**, 1039–1051.

Nyquist, R.A. and Kagel, R.O. (1971) *Infrared Spectra of Inorganic Compounds*. Academic Press, New York and London.

Orberger, B., Gallien, J.P., Pinti, D.L., Fialin, M., Daudin, L., Grocke, D.R. and Pasava, J. (2005) Nitrogen and carbon partitioning in diagenetic and hydrothermal minerals from Paleozoic Black Shales, (Selwyn Basin, Yukon Territories, Canada). *Chemical Geology*, **218**, 249–264.

Parker, J.H., Feldman, D.W. and Ashkin, M. (1967) Raman scattering by silicon and germanium. *Physical Review*, **155**, 712–714.

Raith, M., Devaraju, T. and Spiering, B. (2014) Paragenesis and chemical characteristics of the celsian−hyalophane−K-feldspar series and associated Ba–Cr micas in barite-bearing strata of the Mesoarchaean Ghattihosahalli Belt, Western Dharwar Craton, South India. *Mineralogy and Petrology*, **108**, 153–176.

Reinecke, T. (1982) Cymrite and celsian in manganese-rich metamorphic rocks from Andros Island-Greece. *Contributions to Mineralogy and Petrology*, **79**, 333–336.

Russell, M., Hall, A., Willan, R., Allison, I., Anderton, R. and Bowes, G. (1984) On the origin of the Aberfeldy celsian + baryte + base-metal deposits, Scotland. Pp. 159–170 in: *Prospecting in Areas of Glaciated Terrain 1984*. Institution of Mining and Metallurgy, London.

Sakamoto, J., Hashimoto, S., Tsuda, T., Sugahara, T., Inoue, Y. and Ohgaki, K. (2008) Thermodynamic and

Raman spectroscopic studies on hydrogen plus tetra-n-butyl ammonium fluoride semi-clathrate hydrates. *Chemical Engineering Science*, **63**, 5789–5794.

Sorokhtina, N., Chukanov, N., Voloshin, A., Pakhomovsky, Y.A., Bogdanova, A. and Moiseev, M. (2008) Cymrite as an indicator of high barium activity in the formation of hydrothermal rocks related to carbonatites of the Kola Peninsula. *Geology of Ore Deposits*, **50**, 620–628.

Smith, J.V. and Brown, W.L. (1988) *Feldspar Minerals, Volume 1: Crystal Structures, Physical, Chemical, and Microtextural Properties*. Springer, Berlin, Heidelberg.

Stefov, V., Soptrajanov, B., Kuzmanovski, I., Lutz, H.D. and Engelen, B. (2005) Infrared and Raman spectra of magnesium ammonium phosphate hexahydrate (struvite) and its isomorphous analogues. III. Spectra of protiated and partially deuterated magnesium ammonium phosphate hexahydrate. *Journal of Molecular Structure*, **752**, 60–67.

Steiner, M., Wallis, E., Erdtmann, B.D., Zhao, Y.L. and Yang, R.D. (2001) Submarine-hydrothermal exhalative ore layers in black shales from South China and associated fossils – insights into a Lower Cambrian facies and bio-evolution. *Palaeogeography Palaeoclimatology Palaeoecology*, **169**, 165–191.

Viswanathan, K. and Kielhorn, H.M. (1983) Variations in the chemical-compositions and lattice dimensions of (Ba,K,Na)-feldspars from Otjosondu, Namibia and their significance. *American Mineralogist*, **68**, 112–121.

Wang, J. and Li, Z.X. (2003) History of Neoproterozoic rift basins in South China: implications for Rodinia break-up. *Precambrian Research*, **122**, 141–158.

Wang, J.G., Chen, D.Z., Wang, D., Yan, D.T., Zhou, X.Q. and Wang, Q.C. (2012) Petrology and geochemistry of chert on the marginal zone of Yangtze Platform, western Hunan, South China, during the Ediacaran–Cambrian transition. *Sedimentology*, **59**, 809–829.

Whitney, D.L. and Evans, B.W. (2010) Abbreviations for names of rock-forming minerals. *American Mineralogist*, **95**, 185–187.

Xia, F., Ma, D., Pan, J., Chen, S., Cao, S., Sun, Z., Liu, C. and Guo, G. (2005) EMP study of early Cambrian barite deposits in Eastern Guizhou, China. *Acta Mineralogica Sinica*, **25**, 289–294.

Yang, A., Zhu, M., Zhang, J., Zhao, F. and Lv, M. (2015) Sequence stratigraphic subdivision and correlation of the Ediacaran (Sinian) Doushantuo Formation of Yangtze Plate, South China. *Journal of Palaeogeography*, **17**, 1–20.

Zhu, M. (2004) Biological and geological processes of the Cambrian explosion: evidence from the Yangtze Platform of South China introduction. *Progress in Natural Science*, **14**, V–X.